NASA Contractor Report 201583

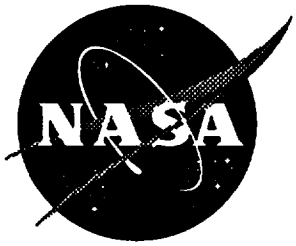

Using Fast-Steering Mirror Control to Reduce Instrument Pointing Errors Caused by Spacecraft Jitter

Thomas A. Johnson, Jeffery Antol, Ted M. Holtz, and Vince Cuda
CTA Incorporated, Hampton, Virginia

Contract NAS1-18936

June 1996

National Aeronautics and
Space Administration
Langley Research Center
Hampton, Virginia 23681-0001

Table Of Contents

List of Figures

List of Tables

Introduction

The control of spacecraft structures involves the analysis, characterization, and control of spacecraft dynamics. Previously, CTA performed a study to identify on-board disturbances of a small satellite (SmallSat) and their effect upon pointing jitter (ref. NASA CR-194915). Jitter is defined as the maximum angular displacement of a particular point on the spacecraft over a given period of time (known as the jitter window). In order to enhance the optical resolution of space borne imaging systems, many approaches to reduce this jitter are being considered for use by SmallSats. Traditional methods apply control technologies to on-board disturbances at their point of origin. This method is useful when disturbances are well defined and the number of disturbances are few. A second approach is the correction of the optical image through active compensation at the instrument. One such method is the use of a fast steering mirror (FSM) to reduce instrument pointing error caused by spacecraft jitter. Existing spacecraft (i.e., GOES 8) use a FSM with feed-forward control to compensate for deterministic pointing errors. Feed-forward compensation can be successful if the on-board disturbances are well known. The focus of this study is the use of a FSM with feed-back control and the application of this technology to a generic SmallSat mission. This approach should provide broadband compensation without requiring apriori knowledge of the on-board disturbances.

Scope of this Study

The scope of this study was to investigate the benefit of using feedback control of a FSM to reduce instrument pointing errors. Initially, the study identified FSM control technologies and categorized them according to their use, range of applicability, and physical requirements. Candidate payloads were then evaluated according to their relevance in use of fast steering mirror control technologies. This lead to the mission and instrument selection which served as the candidate mission for numerical modeling. A standard SmallSat was designed in order to accommodate the payload requirements (weight, size, power, etc.). This included sizing the SmallSat bus, sizing the solar array, choosing appropriate antennas, and identifying an attitude control system (ACS). A feedback control system for the FSM compensation was then designed, and the instrument pointing error and SmallSat jitter environment for open-loop and closed-loop FSM control were evaluated for typical SmallSat disturbances. The results were then compared to determine the effectiveness of the FSM feedback control system.

Acknowledgments

CTA would like to acknowledge the efforts of David Cox of NASA Langley Research Center's (LaRC) Guidance and Control Branch for developing the FSM control algorithms. The success of this study is directly associated with the capability of the FSM control laws. CTA would also like to recognize Sean Kenny and Dr. Peiman Maghami for their assistance with the PLATSIM software.

Fast Steering Mirror Technology

A FSM is an electro-mechanically actuated reflecting surface that can be used to counteract vibration disturbances before an image reaches the optics of an instrument. FSMs are used for rapid scanning of a target to maintain line of sight. These devices have several inherent attributes including: low weight, power, and volume; low moments of inertia; high bandwidth (0.5 to 2 kHz); fast response (3 to 10 ms); fine resolution (< 0.1 arcsec); smooth motion; and small reaction torque. Many of these attributes conflict with each other, and trades between them may be required to meet instrument requirements. Although these devices can be used to steer a few degrees off-axis, bandwidth or power may be traded for higher excursion angles. A feedback control loop is used to compensate for platform motion and vibrations to provide an optically correct image to the receiving optical instrument.

Several companies have conducted research into the control of FSMs for various missions ranging from ground-based, to airborne, to space-based. For this study, a FSM was required that had a slew angle greater than 6 degrees to allow scanning as well as jitter reduction. The mirror design chosen for use in this study is similar to one manufactured by Ball Communications Systems, for an airborne reconnaissance platform. Its size and performance is compatible with the instrument selected for this study. Table 1 shows the instrument specifications, while Figure 1 and Figure 2 display the overall dimensions of the FSM. The mechanism will direct, scan, and stabilize a two inch beam over a total angular range of eight degrees at a scan rate of 15 Hz. The instrument chosen for this study has a requirement of 6 degrees at a scan frequency less than 1 Hz.

Table 1: Ball FSM Specifications

Jitter	0.9 arc sec
Accuracy	± 6.8 arc sec
Pitch excursion	± 4.4 degrees
Yaw excursion	± 1.5 degrees
Clear aperture	5.6 cm x 7.9 cm
Weight	1.2 kg

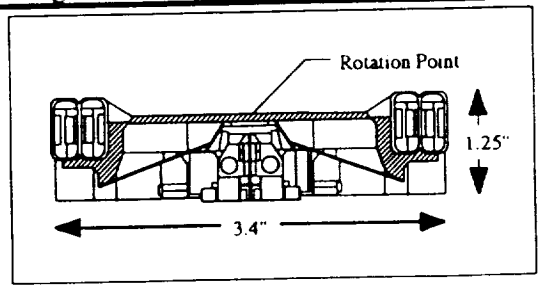

Figure 1: Side View of Ball's FSM

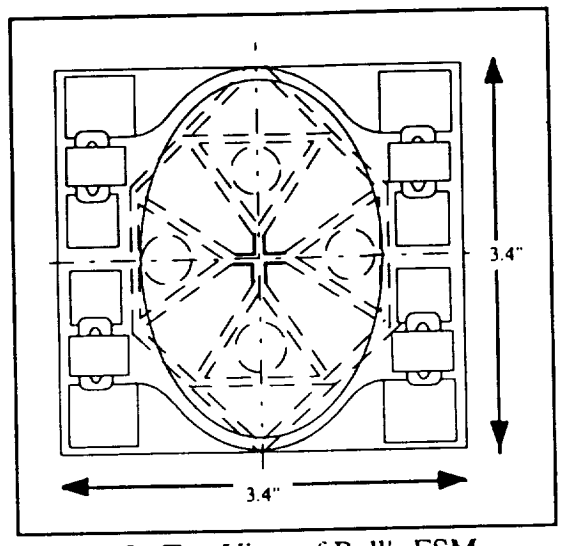

Figure 2: Top View of Ball's FSM

The benefits of using a FSM in the optical path of an instrument are that a stable image can be presented to the instrument, without concern for spacecraft jitter. Other methods of reducing jitter are to use larger more robust momentum wheels or a more sophisticated attitude control system (ACS). This solution reduces the power, cost, and weight associated with reducing jitter. It is easier to correct for spacecraft jitter in the optical path, than to completely remove jitter from the spacecraft. This allows instruments with FSM control to meet pointing requirements, even though the spacecraft bus is vibrating. This could be a real advantage for multi-instrument bases.

Mission Definition

Mission definition consisted of selecting a spacecraft bus, instrument, and control technology. With the exception of the control technology, other mission parameters were not considered critical, but served to fill out the description of the mission scenario. With these constraints, the power requirements served as one of the critical mission resources and the solar arrays were sized to accommodate the resource needs and fit within a Pegasus class vehicle shroud. This arrangement served as a worst case scenario since other launch options provided more volume for the folded arrays. Instrument selection required a proven optical instrument that monitored the visible or near-visible light spectrum. To perform this study, candidate spacecraft and payloads were identified and categorized according to their compatibility with the mission objectives. Upon selection of the payload, the spacecraft bus was chosen and resources required for mission operation were identified. Upon hardware selection, the orbital parameters were chosen to meet current instrument science objectives.

Instrument Selection

Thirty-eight payloads were considered from the Earth observing community, and their requirements were matched to spacecraft resources of a standard CTA Space Systems (CTASS) bus. EOS payloads were the best candidates for this study, because they have flown on numerous occasions, have heritages that are several generations long, and the requirements are defined sufficiently for inclusion into the computational modeling phase of this study. From the set of candidate payloads, a representative instrument was selected. The major criteria of instrument selection included weight, power, and volume resource requirements. Of these, only one optical payload had the required imaging hardware that may benefit from FSM technology.

The Stratospheric Aerosol and Gas Experiment III (SAGE III) was selected as the payload for this study. SAGE III is an Earth limb-scanning grating spectrometer that obtains global profiles of aerosols, O_3, H_20, NO_2, NO_3, OCLO, clouds, temperature, and pressure in the mesosphere, stratosphere, and troposphere. SAGE III is a natural and improved extension of the successful Stratospheric Aerosol Measurement II (SAM II), SAGE I, and SAGE II experiments. The SAGE III payload requirements are shown in Table 2.

The major selection criterion for the instrument was that the payload was an imaging instrument and that it could benefit from the application of FSM technology. Several payloads fit this category, but only the SAGE III was considered for final selection. SAGE III currently is being considered for several flight opportunities, it is a light weight instrument, and other instrument resource requirements are well suited to the CTASS bus design. Upon selection of this instrument, resources for the mission could be firmly established.

Table 2: Sage III Requirements

Requirements	SAGE III
Physical Dimensions	35 cm dia., 75 cm len. - sensor assembly 25 cm x 19 cm x 35 cm - electronics package
Mass	26 kg - sensor assembly 14 kg - electronics package
Power (nominal/peak)	20/60 Watts
Thermal Rejection (nominal/peak)	20/60 Watts
Orbital altitude	601 km
Orbital inclination	57 - 66 degrees
Duty Cycle	6+ minutes/orbit
Data throughput	100 Kbits/second
Data storage	100 Megabits
Lifetime	5 years

Orbit Selection

In order to size the solar arrays and predict the solar array thermal snap torque, a specific spacecraft orbit was chosen. The orbit parameters were selected based upon the payload requirements and are presented in Table 3. Figure 3 graphically depicts the spacecraft orbit.

Table 3: Orbital Parameters

Parameter	Value
Altitude	601 km
Orbital Period	96.69 minutes
Inclination	57.00 degrees
Eccentricity	0
Max. Umbra	35.50 minutes
Sun Fraction	0.63
Max. Beta	80.4 degrees

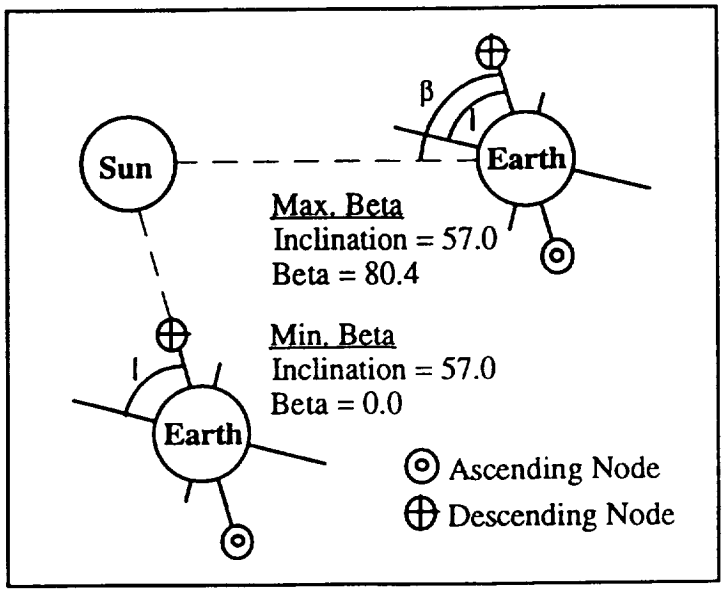

Figure 3. Spacecraft Orbit

Spacecraft Description

The selection of the SmallSat to host the SAGE III payload consisted of choosing a spacecraft bus, sizing the solar arrays, and selecting appropriate antennas. Figure 4 shows the overall dimensions of the spacecraft and payload, while Table 4 details the weight and dimensions of each component.

Table 4. Spacecraft Specifications

Element	Weight (lbs)
CTASS Bus (includes ACS)	201.00
SAGE Sensor Assembly	57.33
SAGE Electronics	30.87
Star Trackers (3)	68.30
Solar Arrays (2)	39.30
Solar Array Supports (2)	0.66
Antennas (4)	1.32
Stiffeners	0.00
Total	398.78

* Total SAGE Payload weight is 88.20 lbs

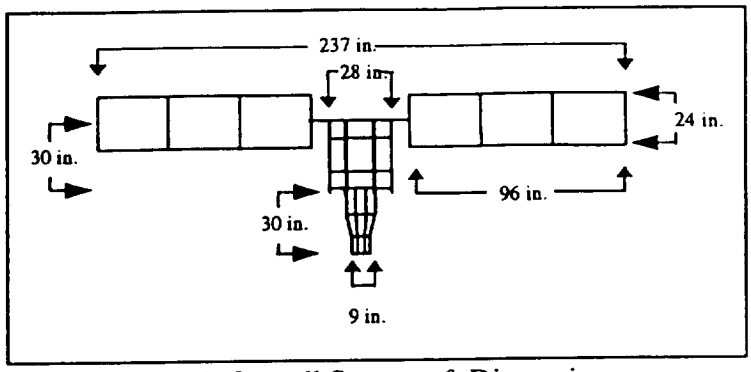

Figure 4: Overall Spacecraft Dimensions

Spacecraft Bus

Selection of the spacecraft bus was based upon two criteria: bus capability to meet payload resource requirements and availability of bus specifications at the time of this study for use in the computational modeling. An eight-sided CTASS bus was selected to represent a typical SmallSat, because the bus can accommodate many of the payloads considered for this study and the bus specifications were readily available. A wire-frame drawing of the SmallSat bus, as modeled in MSC NASTRAN, is shown in Figure 5.

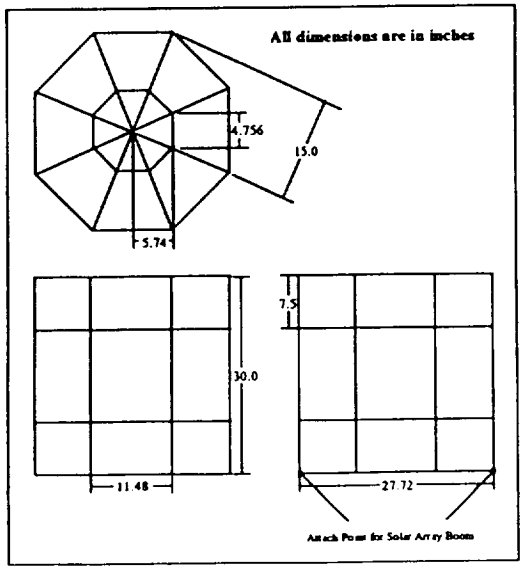

Figure 5. CTASS Spacecraft Bus Dimensions

Solar Array Sizing

Because of the combined payload and spacecraft power requirement, and the high beta angles, a sun-tracking solar array was chosen to power the spacecraft. A power analysis was performed to determine the size of the array. Solar arrays were sized based on orbit, orbital lifetime, and estimated power requirements. For a 601 km orbit, over five years, using 200 Watts as the minimum End-of-Life (EOL) power, the arrays, shown in Figure 6, were calculated to be: two arrays consisting of three folding sections that are 61 cm x 81.3 cm each, yielding effective array sizes of 61 cm x 244 cm. The total area is 2.97 m^2 providing an EOL power rating of 215 Watts. The equations used to calculate EOL power were provided by CTASS and take into account equipment efficiencies, and environmental degradation. The parameters used for sizing the solar arrays are presented in Table 5.

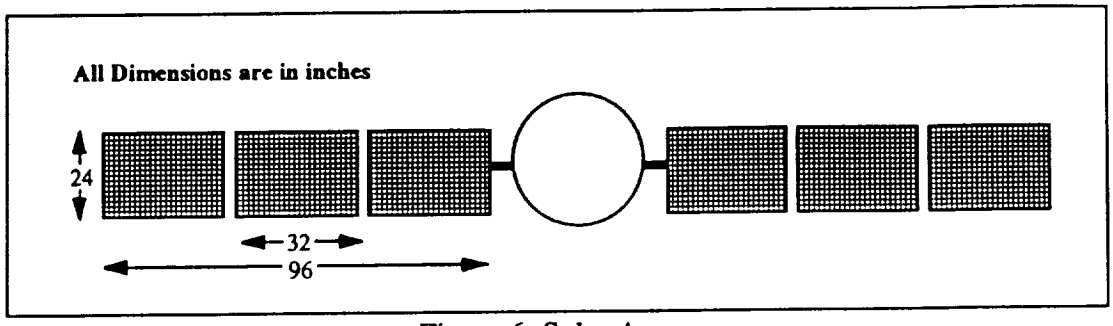

Figure 6: Solar Arrays

Table 5. Factors Used in the Sizing of the Solar Array

Factor	Symbol	Value
Peak Beginning of Life Power Per Unit Area	BOL	0.089 watts/in^2
Payload Power Requirement (Max. sustained)	$P_{navload}$	115 watts
Spacecraft Power Requirement	$P_{s/c}$	100 watts
Thermal Cycle Fatigue	F_{therm}	0.99329 years
UV Exposure	E_{uv}	0.99329 years
Max. Time spacecraft is in the Earth's Umbra	t_{umbra}	35.5 min
Spacecraft's Orbit Period	t_{orbit}	96.69 min
+28 VDC Regulator Efficiency	E_{VDC}	0.93
High Power Switch Efficiency	E_{switch}	0.99
Battery Charge/Discharge Ratio	E_{batt}	0.88
Wiring and Connector (resistive) Loss Efficiency	$E_{w/c\ loss}$	0.99

The following equations were used to calculate the area of the solar array (assuming a 5 year lifetime):

$$\text{Area} = \frac{P_{payload} + P_{s/c}}{BOL * F_{therm}^{5} * E_{uv}^{5} * t_{sun} * E_x * E_{switch} * E_{w/c\ loss}}$$

where

$$E_x = ((E_{VDC} * E_{batt}) * (1 - t_{sun}) + (E_{VDC} * t_{sun}))$$

and

$$t_{sun} = 1 - \frac{t_{umbra}}{t_{orbit}}$$

Antennas

Selection of the antenna was based upon the transmission requirements that include science data downlink, bus telemetry, and uplink. Due to the low transmission requirements (100 kbps science data downlink), a broadband omni-directional system was chosen. The system was assumed to use quadrifilar helix antennas, shown in Figure 7, similar to those on the Multiple Experiments To Earth Orbit and Return (METEOR) spacecraft. Each antenna is 2.5 inches high with a 1 inch diameter and a weight of 150 grams. The antennas are located on four corners of the CTASS Bus, on the nadir side.

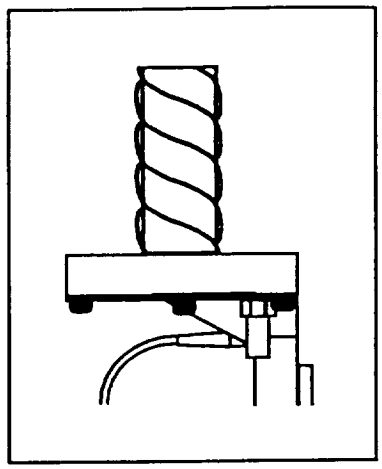

Figure 7: Quadrifilar Helix Antenna

Spacecraft Modeling

The initial step of the computational modeling was to build a finite element model (FEM) of the spacecraft. The results of the finite element analysis (FEA) were used as input to spacecraft simulation. These following sections describe the FEA and spacecraft simulation.

Finite Element Model

A FEM of the spacecraft was developed using the pre-and post- processing tool FEMAP and analyzed using the FEA tool MSC/NASTRAN. The FEM included the spacecraft bus, SAGE III hardware (including the sensor assembly and the electronics package), solar arrays, reaction wheel assembly, star trackers and antennas. The spacecraft bus, SAGE III sensor assembly, reaction wheel assembly, and antennas were modeled as beam elements (CBEAM). The solar arrays were modeled as plate elements (CQUAD4) with non-mass beam elements (CBEAM) added to the edges for stiffness. The star trackers and SAGE III electronics package were modeled as concentrated mass elements (CONM2). The model of the SAGE III mirror structure consisted of beam elements forming a cube, in order to represent several potential orientations of the mirror. Three FEMs were created and analyzed in order to examine potential solar array attitudes: 0, 45 and 90 degrees. The spacecraft modes and mode shapes from the MSC/NASTRAN analysis were used to describe the rigid body and flexible response of the spacecraft in the spacecraft simulation. Initial simulations for each solar array orientation produced similar results. However, the case with the arrays in a 0 degree orientation produced slightly larger responses and therefore, was used for this study. Table 6 shows the mass, center of gravity, and inertias of the SmallSat model and Table 7 shows the modes of the SmallSat (up to 20 Hz), as calculated by MSC/NASTRAN.

Table 6. Spacecraft properties calculated by MSC NASTRAN

Property	Value		
Mass	398.78	(lbs)	
Center of Gravity			
Xcg	0.0		
Ycg	1.72	(inches)	
Zcg	20.22		
Mass Moments of Inertia		(in-lbs sec^2)	
Ixx Ixy Ixz	362166.68	6076.80	206.58
Iyx Iyy Iyz	6076.80	125949.92	495.19
Izx Izy Izz	206.58	495.19	278681.82

Simulation Techniques

The SmallSat analysis focused on identifying the jitter environment for each disturbance source. Platform simulation (PLATSIM) was used to analyze the jitter environment on the SmallSat with and without FSM compensation. Both rigid body and flexible body responses were used for the SmallSat analysis using PLATSIM. Additional MATLAB scripts were written in order to implement the ACS of the SmallSat and the FSM controller.

PLATSIM is a spacecraft simulation developed by NASA LaRC and initially validated for the EOS-AM1 spacecraft. The simulation is written in MATLAB script and incorporates rigid body and flexible body responses of a spacecraft. The spacecraft dynamics are input into the simulation

via the modes and mode shapes of the spacecraft determined by a FEA. Figure 8 shows the processes of the PLATSIM simulation. Torsional forcing functions and axial forces are used to perturb the model. Disturbances are changed by modifying the MATLAB script that describes them. Linear and angular position, velocity, and acceleration at any grid point can be output and jitter can be calculated based on different size time intervals (jitter window).

Table 7: Spacecraft Natural Frequencies

Mode	Frequency (Hz)	Description
1--6	0	Rigid Body Modes
7	1.026	Solar Arrays 1st Bending (in phase)
8	1.540	Solar Arrays 1st Bending (out of phase)
9	3.457	Solar Arrays Support Tubes 1st Bending
10	5.528	Solar Arrays 1st Torsion about Support Tubes (in phase)
11	5.592	Solar Arrays 1st Torsion about Support Tubes (out of phase)
12	6.192	Solar Arrays 2nd Bending (in phase)
13	6.370	Solar Arrays 2nd Bending (out of phase)
14	7.169	Solar Arrays Support Tubes 2nd Bending
15	16.824	Solar Arrays 3rd Bending (in phase)
16	16.852	Solar Arrays 2nd Torsion about Support Tubes (in phase)
17	16.870	Solar Arrays 2nd Torsion about Support Tubes (out of phase)
18	16.895	Solar Arrays 3rd Bending (out of phase)

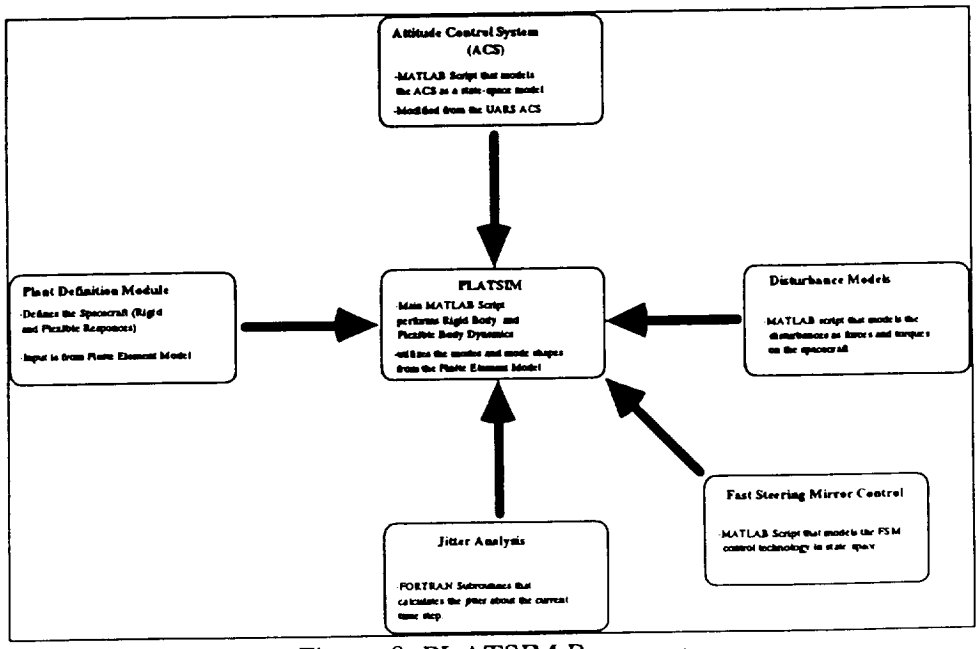

Figure 8: PLATSIM Processes

SmallSat Disturbances

The SmallSat analysis concentrated on determining the effect of individual disturbances upon the spacecraft. The following disturbances were analyzed: the thermal snap of the solar arrays, the solar array harmonic drive, and the dynamic imbalance of the momentum wheels. The effect of these disturbances upon the SmallSat was derived as a set of forcing functions in roll, pitch, and yaw. Forcing functions are derived as a set of axial forces and torques about each axis. These forcing functions were used to perturb the simulation. A description and derivation of each disturbance are presented in the following sections.

Thermal Snap

The model of the disturbance caused by the thermal snap of the solar array as it enters and leaves the penumbra is based upon a similar analysis performed for the UARS solar array. For this type of an array, the thermal snap is more of a bending phenomena caused by the temperature difference across the illuminated and dark side of the solar array panel as the spacecraft moves from night to day, and from day to night. The forcing function which describes the spacecraft torsional disturbance caused by the thermal snap of the solar array is calculated as follows:

$$\text{TROLL} = -\text{Tn} * \text{COS}(\text{PANG} * \frac{2\pi}{360})$$

$$\text{TPITCH} = 0$$

$$\text{TYAW} = \text{Tn} * \text{SIN}(\text{PANG} * \frac{2\pi}{360})$$

Tn - Torque normal to the solar array (ft lb)

PANG - Angle that the normal of the solar array makes with the sun (degrees)

The Torque normal to the solar array panel (T_n) can be expressed as follows:

$$T_n = \frac{T_{mag} * t_d}{t_r * (t_p - t_r)} * (sign + FAC)$$

Tmag - Magnitude of the reference torque (ft lb)

t_d - decay time of exponential function (sec)

t_r - rise time (sec)

t_p - time spent in penumbra (sec)

The values for SIGN and FAC are defined for each time interval of the thermal snap. The four intervals characterize the rise of the thermal snap force, an exponential decay, a rise in the force in the opposite direction, and an exponential decay, respectively.

$[0<t<t_r]$

$$\text{FAC} = -\text{EXP}(\frac{-t}{td})$$

$$\text{SIGN} = 1$$

$[tr<t<(tp-t_r)]$

$$\text{FAC} = -\text{EXP}(\frac{-t}{td}) + \text{EXP}(\frac{-(t-tr)}{td})$$

$$\text{SIGN} = 0$$

$[(t_p-t_r)<t<t_p]$

$$\text{FAC} = -\text{EXP}(\frac{-t}{td}) + \text{EXP}(\frac{-(t-tr)}{td}) + \text{EXP}(\frac{-(t-tp+tr)}{td})$$

$$\text{SIGN} = -1$$

$[t_p<t]$

$$\text{FAC} = -\exp(\frac{-t}{td}) + \exp(\frac{-(t-tr)}{td}) + \exp(\frac{-(t-tp+tr)}{td}) - \exp(\frac{-(t-tp)}{td})$$

$$\text{SIGN} = 0$$

The parameters used for modeling thermal snap, shown in Table 8, are based on the selected orbit and solar arrays. The resulting thermal snap disturbance model, shown in Figure 9, is modeled mathematically as follows:

$(0<t\leq 0.2)$

$$T_{ROLL} = 0.0184*(1-e^{-t/8.457})$$
$$T_{YAW} = 0.0429*(1-e^{-t/8.457})$$

$(0.2<t\leq 9.10)$

$$T_{ROLL} = 0.0184*(-e^{-t/8.457}+e^{0.2-t/8.457})$$
$$T_{YAW} = 0.0467*(-e^{-t/8.457}+e^{0.2-t/8.457})$$

$(9.10<t\leq 9.30)$

$$T_{ROLL} = 0.0184*(-1-e^{-t/8.457}+e^{(0.2-t)/8.457}+e^{(9.1-t)/8.457})$$
$$T_{YAW} = 0.0467*(-1-e^{-t/8.457}+e^{(0.2-t)/8.457}+e^{(9.1-t)/8.457})$$

$(9.30<t<1000)$

$$T_{ROLL} = 0.0184*(-e^{-t/8.457}+e^{(0.2-t)/8.457}+e^{(9.1-t)/8.457}-e^{(9.3-t)/8.457})$$
$$T_{YAW} = 0.0467*(-e^{-t/8.457}+e^{(0.2-t)/8.457}+e^{(9.1-t)/8.457}-e^{(9.3-t)/8.457})$$

Table 8. Parameters Used in developing the Thermal Snap Model

Factor	Symbol	Value
Rise time of force (sec)	tr	0.2
Time spent in penumbra (sec)	tp	9.3
Decay time of exponential function (sec)	td	8.457
Tmag - Magnitude of the reference torque (ft lb)	Tmag	8.3728e-004
Angle that the normal of the solar array makes with the sun (degrees)	Pang	113.25

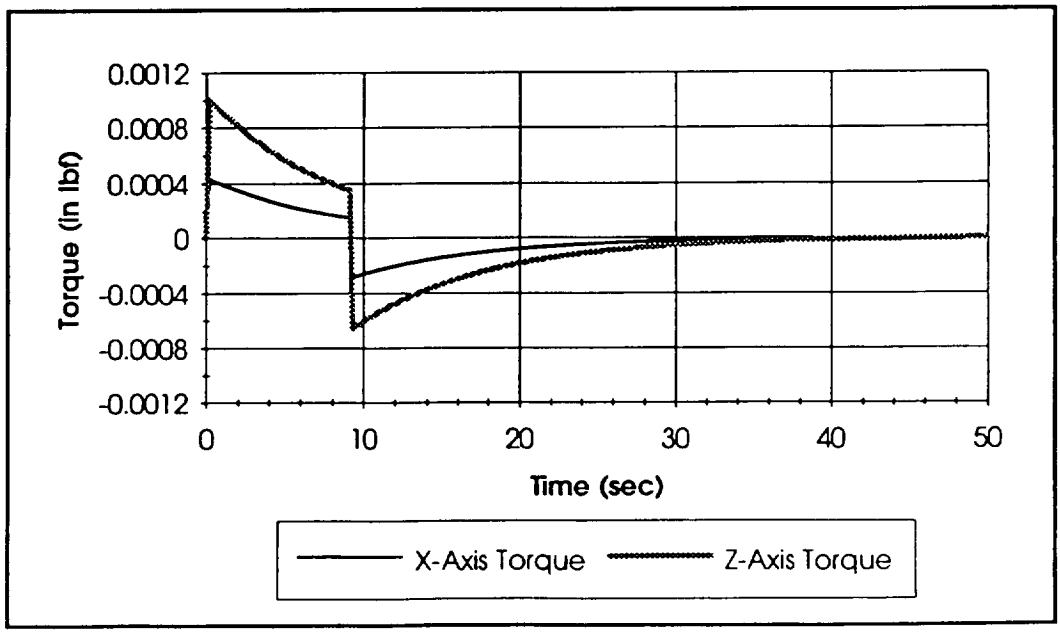

Figure 9: Thermal Snap Disturbance

Solar Array Harmonic Drive Model

The model of the disturbance caused by the solar array harmonic drive is based upon a similar analysis performed for the EOS AM1 and UARS harmonic drives. For the analysis, it is assumed

that the solar array rotates at a constant rate and that the torque variations induced on the spacecraft by the harmonic drive are sinusoidal. It is also assumed that the parameters of the harmonic drive are equal to those for the UARS harmonic drive, except for changes in inertia due to the size of the arrays. Figure 10 depicts the model of the solar array harmonic drive.

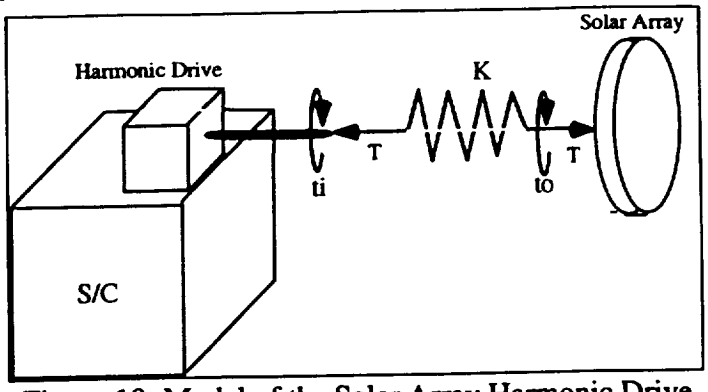

Figure 10: Model of the Solar Array Harmonic Drive

The forcing function which describes the torsional disturbance of the solar array harmonic drive is represented by a magnitude (T_{HD}) and a frequency (ω_{HD}). The torsional disturbance results from a periodic position error of the harmonic drive. This position error is depicted in Figure 11. The position error of the harmonic drive is characterized by the following equation:

$$\Delta\theta = \frac{4}{PD * GR} * \frac{2\pi}{360}$$

$\Delta\theta$ - Drive position error (rad); difference between actual and desired position

GR - gear ratio of the harmonic drive (nd)

PD - period (per degrees)

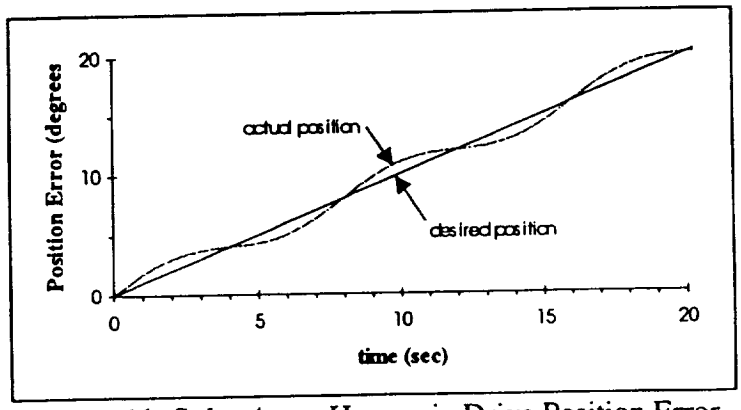

Figure 11: Solar Array Harmonic Drive Position Error

The magnitude of the harmonic drive disturbance is calculated as follows:

$$T_{HD} = K * \Delta\theta$$

where

$$K = J * \omega_{SA}^2$$

K - Stiffness associated with the solar array (ft-lb/rad)

J - Solar array inertia (slug ft^2)

ω_{sa} - Solar array torsion frequency (rad/sec)

The frequency of the harmonic drive disturbance is calculated as follows:

$$\omega_{HD} = 2 * \left(RPM * \frac{1 \text{ min}}{60 \text{ sec}} \right)$$

ω_{HD} - Frequency of the harmonic drive disturbance (Hz)
RPM - input RPM of the harmonic drive (rev/min)

The parameters used for modeling the harmonic drive disturbance, shown in Table 9, are based on the size of the solar arrays and operating speed of the harmonic drive. The resulting harmonic drive disturbance model, shown in Figure 12, is modeled mathematically as follows:

$(0<t<1000) \quad T_{pitch} = 0.14 * \sin(2 * \pi * 0.23 * t)$

Table 9. Parameters Used in developing the Harmonic Drive Disturbance Model

Factor	Symbol	Value
Gear ratio of the harmonic drive (nd)	GR	6.833
Period (per degrees)	PD	120
Solar array inertia (slug ft^2)	J	3.46
Solar array torsion frequency (rad/sec)	ω_{sa}	6.283
Input RPM of the harmonic drive (rev/min)	RPM	6.9

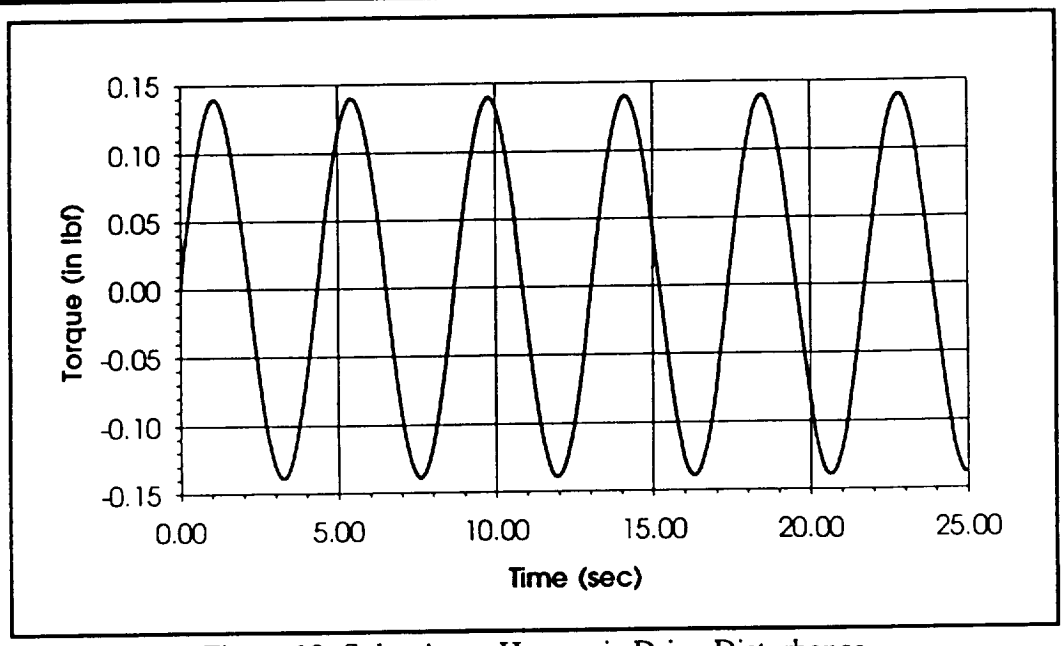

Figure 12: Solar Array Harmonic Drive Disturbance

Momentum Wheel Dynamic Imbalance Model

The model that describes the disturbance caused by a dynamic imbalance of the momentum wheels is based upon measured values of similar momentum wheels. Momentum wheel imbalances are measured for each half of the wheel and are characterized as a point mass at a specific radius. The momentum wheels are modeled after those used by the METEOR ACS. Typical imbalances for the METEOR momentum wheels are characterized as a 25 mg point mass at a 1 inch radius for each half of the wheel. For our analysis, the momentum wheel imbalance is modeled as a single 50 mg point mass at a 1 inch radius. Figure 13 displays the model of the

momentum wheel dynamic imbalance.

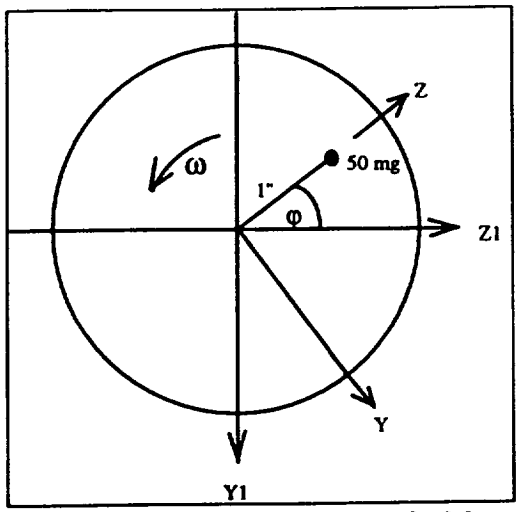

Figure 13: Model of a Dynamic Imbalance of a Momentum Wheel

The forcing function that describes the disturbance caused by the dynamic imbalance of the momentum wheel is calculated as a function of the mass and position of a point mass and the speed that the wheel is rotating. The centrifugal force is coupled with a moment arm to produce a torque at the center of the Reaction Wheel Assembly. The force (F) due to the centrifugal acceleration of the point mass is calculated as follows:

$$F_X = 0$$

$$F_Y = 0$$

$$F_z = m\omega^2 r$$

F - centrifugal acceleration due to the point mass in (X,Y,Z) reference frame (lb)

m - mass of the point mass (slugs)

r - radius of point mass from center of the momentum wheel (ft)

ω - wheel's angular velocity (Hz)

The wheel's angular velocity is calculated as follows:

$$\omega = \frac{H}{I}$$

ω - wheel's angular velocity (Hz)

H - wheel's angular momentum (ft lb sec)

I - wheel's inertia (slug ft^2)

The force (F) is transformed from a reference frame that is fixed to the rotating wheel (X,Y,Z) to the spacecraft reference frame (X1,Y1,Z1), then transformed to a torque by selecting an appropriate moment arm. Table 10 describes the definition of the two reference frames. The transformation of the force F from the (X,Y,Z) reference frame to the (X1,Y1,Z1) reference frame is defined as follows (recall $F_X=F_Y=0$):

$F_{X1} = F_X = 0$

$F_{Y1} = F_Y\cos(\varphi) - F_Z\sin(\varphi) = -F_Z\sin(\varphi)$

$F_{Z1} = F_Z\cos(\varphi) - F_Y\cos(\varphi) = F_Z\cos(\varphi)$

Table 10. Definition of reference frames (X,Y,Z) and (X1,Y1,Z1)

(X,Y,Z) reference frame	(X1,Y1,Z1) reference frame
• X is defined by the rotation of the wheel	• X1 is defined by the rotation of the wheel
• Z is defined by the rotating position of the point mass	• Z1 is defined by the initial position of the point mass
• Y is defined by the right hand rule and the definitions for X and Z	• Y1 is defined by the right hand rule and the definitions for X1 and Z1

The angle φ required for the transformation from the (X,Y,Z) reference frame to the (X1,Y1,Z1) reference frame is calculated as follows:

$$\varphi = \varphi_0 + \dot{\varphi}_0 t + \frac{1}{2}\ddot{\varphi} t^2$$

where

φ - position of the point mass(rad)

φ_0 - initial position of the point mass(rad)

$\dot{\varphi}_0$ - wheel's initial angular velocity(rad / sec)

$\ddot{\varphi}$ - wheel's angular acceleration (rad / sec^2)

The forces F_{X1},F_{Y1},F_{Z1} are converted to torques at the center of the reaction wheel assembly (RWA) as follows:

$$\vec{T} = \vec{r} \times \vec{F}$$

T - Torque due to wheel imbalance in (X1,Y1,Z1) reference frame (ft-lb)

F - Force due to the momentum wheel imbalance in the (X1,Y1,Z1) reference frame (lb)

r - moment arm from the center of the RWA to the force F (ft)

The moment arm for each momentum wheel is illustrated in Figure 14.

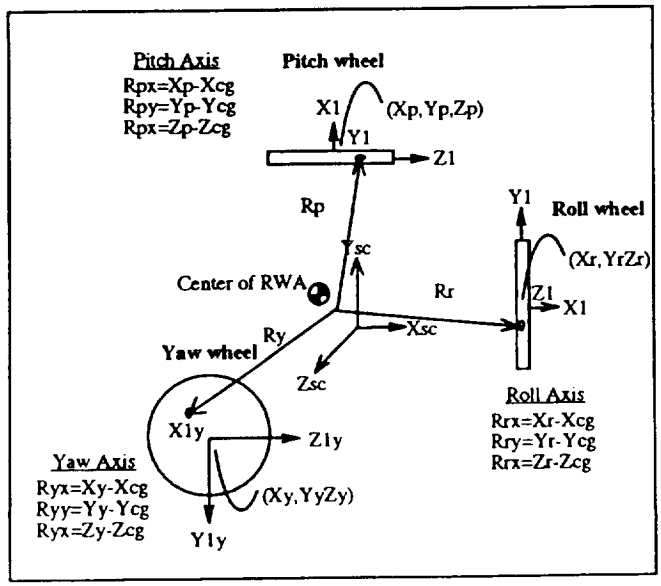

Figure 14: Momentum Wheel Orientations

The parameters used for modeling the dynamic imbalance of the momentum wheels, shown in Table 11, are based on the operating speed and imbalance characteristics of the wheels. The resulting dynamic imbalance disturbance model, shown in Figure 15, is modeled mathematically as follows:

Low RPM	0<t<1000	$T_{ROLL} = 0.00823$ $T_{PITCH} = -0.0494*\cos(2*\pi*7.8*t)$ $T_{YAW} = -0.0494*\sin(2*\pi*7.8*t)$
High RPM	0<t<1000	$T_{ROLL} = 0.00994$ $T_{PITCH} = -0.0594*\cos(2*\pi*8.57*t)$ $T_{YAW} = -0.0594*\sin(2*\pi*8.57*t)$

Table 11. Parameters Used in developing the Dynamic Imbalance Disturbance Model

Factor	Symbol	Value Case 1	Value Case 2
Operating Speed of the momentum wheel (Hz)	ω	8.57	7.8
Mass Associated with the Imbalance (mg)	m	50	50
Location (radius) of the mass associated with the Imbalance (in.)	r	1.0	1.0
Distance from the wheel center to the center of the RWA (in.)	Rrx, Rpy, Ryz	6.0	6.0

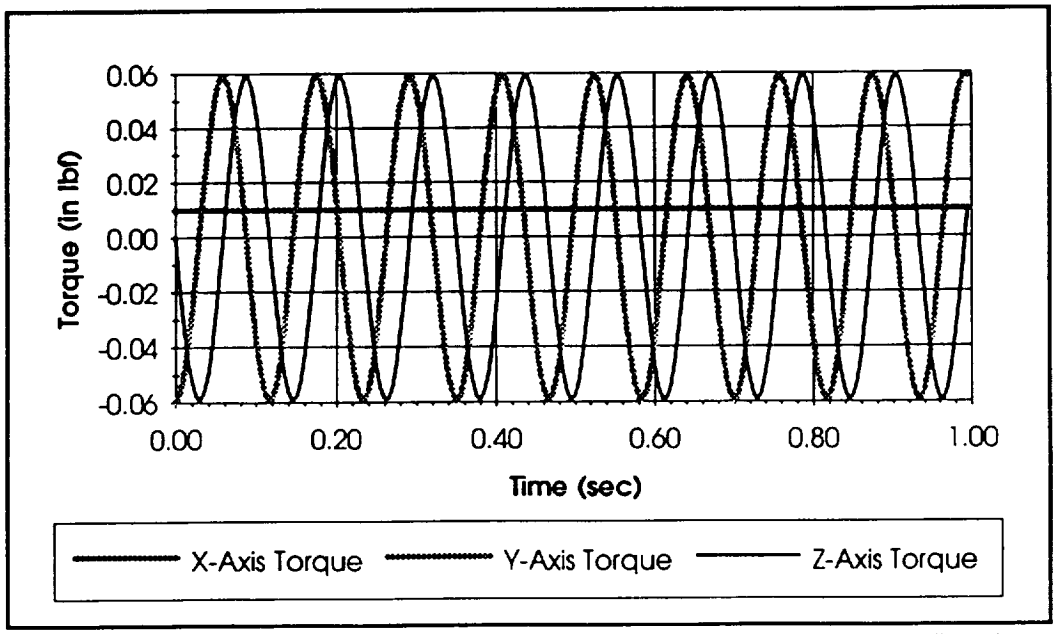

Figure 15: Momentum Wheel Dynamic Imbalance Disturbance (High RPM)

Control Systems

Two control systems were defined for this study. The SmallSat ACS stabilizes the spacecraft and attempts to provide a suitable jitter environment. The FSM controller attempts to counteract any remaining vibrations to further reduce instrument pointing errors. The following sections describe the two control systems.

Attitude Control System (ACS)

Selection of an ACS was based upon two criteria: capability to provide an adequate pointing capability and availability of ACS specifications at the time of this study for use in the computational modeling. The control system used on the Upper Atmosphere Research Satellite (UARS) forms the basis for the ACS used for this study, however, system components were scaled down where feasible (e.g., smaller reaction wheels). Figure 16 provides a graphical representation of the ACS.

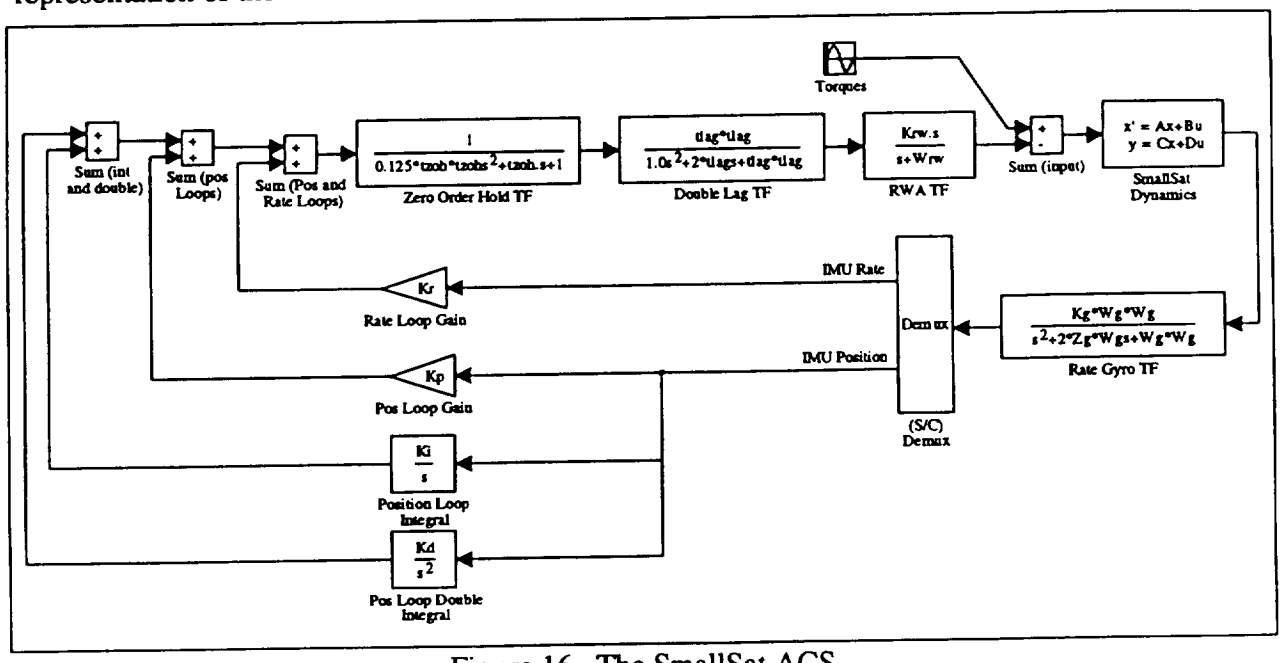

Figure 16. The SmallSat ACS

The selected ACS is a three axis, zero momentum system. The three axis attitude knowledge is provided by an on-board attitude determination system which uses an inertial reference unit to keep track of the spacecraft position in an Earth Centered Inertial (ECI) frame. A star tracker provides periodic updates to correct for gyro drift errors. Ephemeris data is used to construct an Earth pointed target in the ECI frame. Knowing where the spacecraft is pointed and where the spacecraft should point, three axis attitude errors are calculated. The attitude errors are combined with rate, integral, and double integral errors in the controller resulting in inputs to each of three reaction wheels, one in each axis. To prevent wheel saturation, magnetic torquers are used to dump accumulated momentum. A star tracker also provides data to the ACS for calculating gyro drift rates. Table 12 shows a breakdown of the ACS components by mass.

Table 12. ACS Components

Element	Quantity	Weight (lbs)
IMU Electronics	1	6.100
IMU Sensor and Bracket	1	5.200
Horizon Sensor and Bracket	1	6.200
Three Axis Magnetometer	1	0.600
Magnetic Torquer and Bracket	3	16.400
Reaction Wheel and Bracket	4	25.400
ACS Computer	1	11.400
Dual Wheel Driver	2	4.200
Magnetic Torquer Coil and Driver	1	2.200
Total		77.700

Fast-Steering Mirror (FSM) Controller

The FSM control law was developed as an optimal estimator that predicts the boresight jitter environment on-board the SmallSat from the Inertial Measurement Unit (IMU) position and rate information, as well as high bandwidth measurements from the Attitude Determination Sensors (ADS). The ADS is a fluidic device which measures angular displacements over a bandwidth of 2 Hz to 1000 Hz. The estimator combined this measurement with the low frequency response of the IMU's to provide a jitter estimate which was valid over a large frequency range. The jitter estimate was used to drive the FSM servo loop, which acted to cancel the effect of jitter on the optical boresight. In designing the estimator a model of the spacecraft was constructed which contained the first 20 flexible modes. Since the spacecraft model contained no translational actuators or sensors, internal balancing was used to remove the uncontrollable and unobservable rigid-body translation modes from the six coupled rigid body modes of the NASTRAN model. To form a model for the estimator design, the first 20 flexible modes were combined with the rotational dynamics and augmented with sensor and actuator dynamics. Linear Quadratic Gaussian (LQG) estimator theory was applied to this model with noise statics chosen to tailor the estimator's bandwidth. A reduced order estimator was derived from the LQG estimator by applying balancing and then truncating the lightly observable states.

A FSM servo controller was designed separately, using classical techniques, to provide unity gain and flat phase response for the mirror over a bandwidth of about 25 Hz. Outputs of the FSM model were mirror position and reaction torques. The position was used to compensate for boresight jitter, and reaction torques allowed the simulation to include the disturbance effect of the mirror's motion.

Figure 17 shows a block diagram of the closed-loop system. The SmallSat dynamics is simply a state-space representation of the NASTRAN model. It has disturbance torques and reaction wheel torques as its inputs and angular displacements at the boresight, ADS and IMU locations, and angular rates at the IMU location as its outputs. Sensor and actuator dynamics were modeled independently and augmented to the system, as shown in Figure 17. Position outputs from the FSM servo-loop were used for tip and tilt corrections to boresight pointing, and reaction torques applied as disturbances to the spacecraft model.

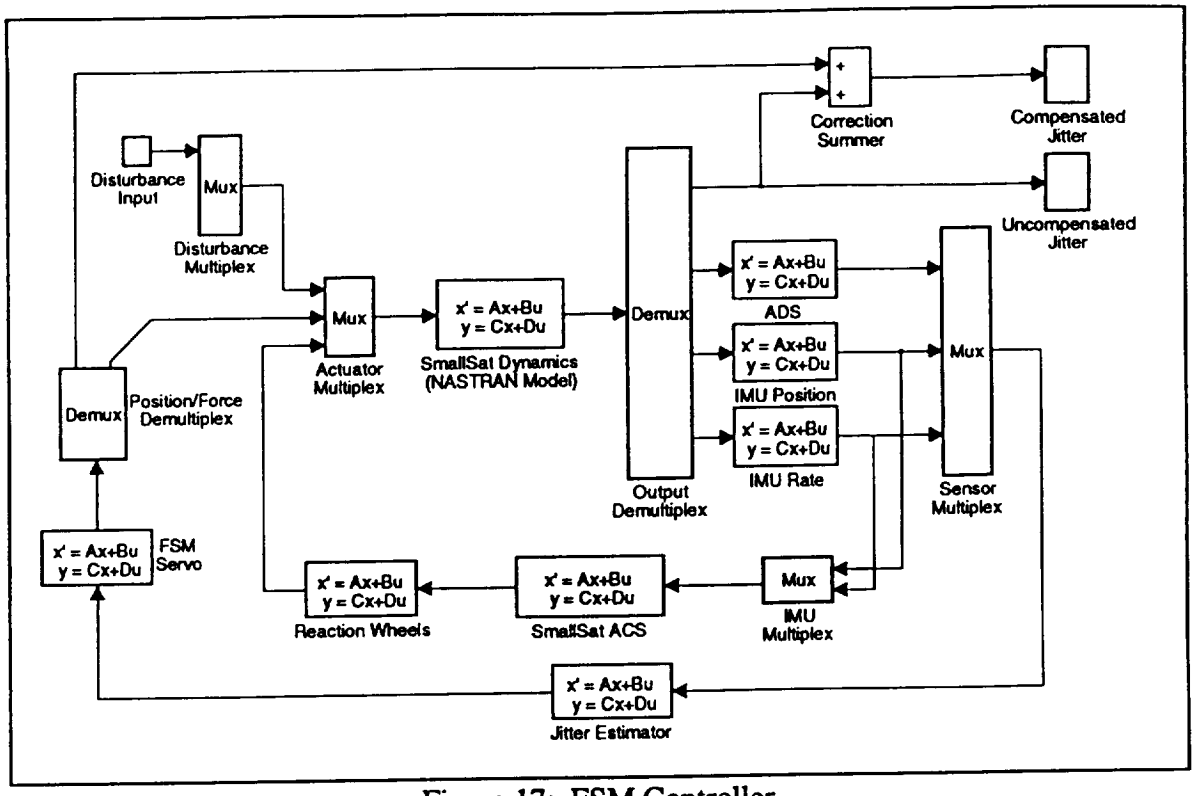

Figure 17: FSM Controller

Disturbance sources are primarily from the reaction wheel imbalance and motion of the solar arrays. Therefore the reaction wheel locations and the attachment point of the two solar arrays to the spacecraft bus are the most significant disturbance locations. The performance output is the compensated spacecraft jitter in roll and yaw. Since there are a total of nine disturbance inputs and two outputs, 18 bode plots are required to describe the possible disturbance paths. Instead, presented in Figure 18 and Figure 19 are the open-loop and closed-loop maximum singular value plots for the reaction wheel inputs and solar array inputs taken as a set. This represents the largest possible gain between the input and output vector spaces as a function of frequency, and provides a worst case bound on all possible disturbance sources. From these plots it can be seen that vibration attenuation from the control law is very good at low frequencies, poorer above the bandwidth of the actuator, and essentially open-loop at high frequencies.

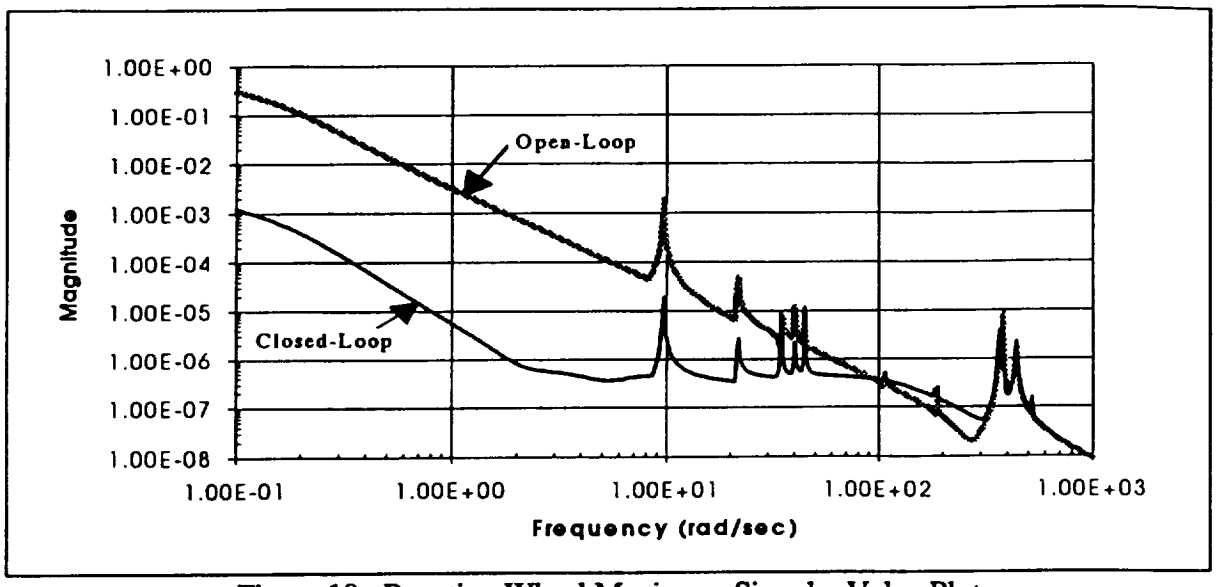

Figure 18: Reaction Wheel Maximum Singular Value Plot

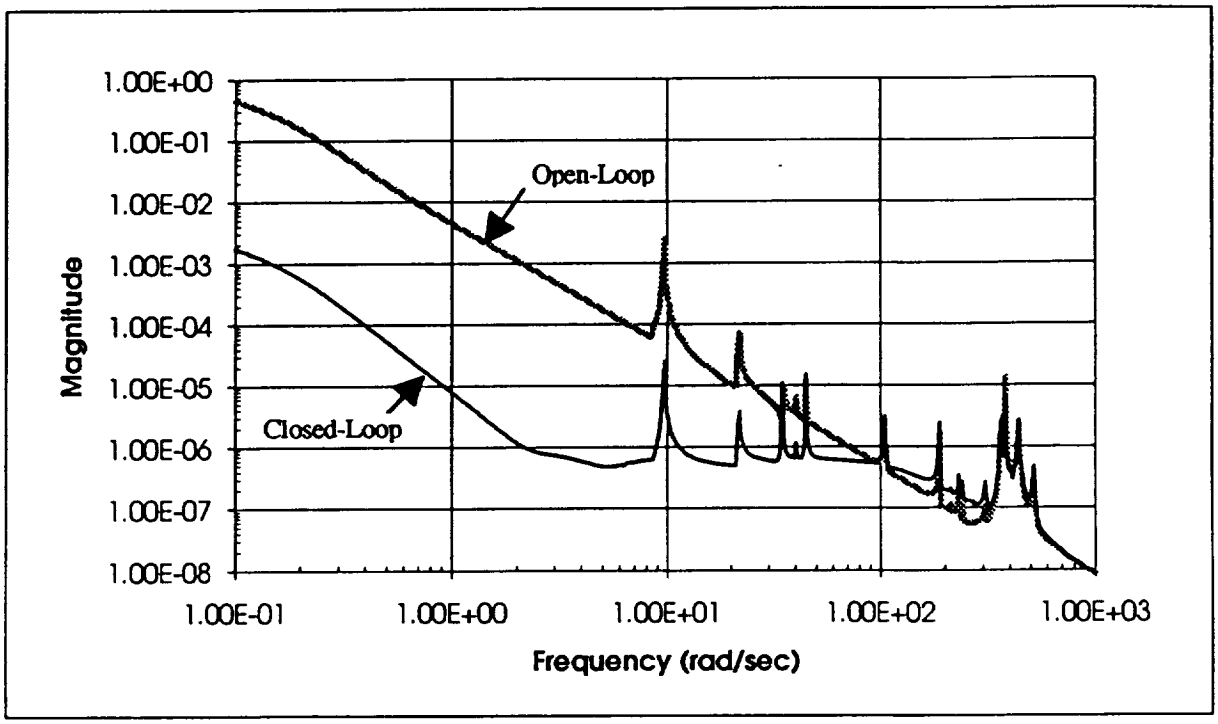

Figure 19: Solar Array Maximum Singular Value Plot

SmallSat Analysis

The SmallSat analysis concentrated on determining the effect of utilizing FSM feedback control to reduce the instrument pointing error (boresight jitter). Open-loop and closed-loop analyses were performed in order to evaluate the benefit of this technology. The open-loop SmallSat simulation was performed to baseline the results of the FSM closed-loop analysis. The ACS provided the only jitter compensation for the open-loop simulation. The simulation for the closed loop-analysis included the FSM control algorithms for additional jitter suppression, and also accounted for the reaction torque produced by the FSM as it compensates for the spacecraft's jitter. Since this is an additional disturbance on the SmallSat, its effect on the SmallSat and other instruments was also evaluated. The following relation was used to characterize the reduction or increase in jitter between the open-loop and closed-loop analyses.

$$dB = 20 * \log\left(\frac{JITTER_{closed-loop}}{JITTER_{open-loop}}\right)$$

The following SmallSat disturbances were analyzed; solar array harmonic drive, thermal snap of the solar array, and the dynamic imbalance of the momentum wheels. The dynamic imbalance of the momentum wheels was analyzed at two operating frequencies (low RPM - 7.8 Hz and high RPM - 8.6 Hz). Jitter was calculated as the maximum angular displacement of a particular point on the spacecraft over a 1 second jitter window. The maximum jitter experienced by the SmallSat after the a steady state response was reached was reported. The only exception was the thermal snap disturbance, because it is a transient event. Time histories of the simulation results are presented in Appendix A.

FSM Performance on Instrument Pointing Error

Table 13 presents the results of the open-loop and closed-loop analyses and the reduction in the pointing error (in decibels) achieved by utilizing a FSM. The FSM provides jitter compensation for displacements about the roll and pitch axis. Differences in the open-loop and closed-loop yaw axis results are attributed to the cross-product terms of the SmallSat's inertia and an application of reaction torques about the roll and pitch axis caused by the FSM. The results show a relatively small increase in the pointing error about the uncontrolled yaw axis (less than 0.25 dB). The harmonic drive produces the largest disturbance on the SmallSat (122.35 arcsec/sec about the pitch axis). FSM compensation reduces the instrument pointing error about the pitch axis produced by the harmonic drive disturbance to 0.195 arcsec/sec (a 55 dB reduction). A 40-55 dB reduction in pointing error about the roll and pitch axis is realized for the harmonic drive and thermal snap disturbances. The reduction in pointing errors is smaller (8-11 dB) for the higher frequency disturbances (momentum wheel imbalance), however, the magnitudes of these disturbances are smaller and have less impact on the SmallSat. The overall reduction in instrument pointing error realized for all the disturbances is 24-36 dB about the roll axis and 38-54 dB about the pitch axis. Because noise was not introduced into the simulation, the reduction in jitter is below the noise floor of available sensors and below the fidelity of the FSM servo loops. A more detailed investigation would include these effects, however, the conclusion from this proof-of-concept study is that feedback control of an FSM provides substantial reduction in instrument pointing.

Table 13. Instrument Pointing Error

Disturbance	Open-Loop (arcsec/sec)			Closed-Loop (arcsec/sec)			Pointing Error Reduction (dB)		
	Roll	Pitch	Yaw	Roll	Pitch	Yaw	Roll	Pitch	Yaw
Harmonic Drive	1.833	112.350	0.208	0.019	0.195	0.213	-39.82	-55.22	0.21
Thermal Snap	0.813	0.054	2.462	0.005	0.000	2.464	-44.23	-42.54	0.01
Momentum Wheel									
X-axis only (Low RPM)	0.002	0.032	0.332	0.001	0.010	0.335	-8.15	-10.33	0.09
X-axis only (High RPM)	0.002	0.031	0.178	0.001	0.011	0.180	-5.11	-8.99	0.11
All 3 Axis (Low RPM)	0.059	0.068	0.665	0.016	0.021	0.676	-11.17	-10.24	0.14
All 3 Axis (High RPM)	0.054	0.064	0.356	0.019	0.023	0.363	-9.29	-8.84	0.16
All Disturbances									
Random-Phase (Low RPM)	2.669	112.436	3.028	0.035	0.196	2.352	-37.67	-55.16	-2.20
Random-Phase (High RPM)	2.684	112.429	2.898	0.037	0.204	2.193	-37.19	-54.83	-2.42
In-Phase (Low RPM)	2.705	112.471	3.336	0.040	0.216	3.353	-36.62	-54.33	0.05
In-Phase (High RPM)	2.700	112.468	3.027	0.042	0.218	3.040	-36.10	-54.24	0.04

* Low RPM and High RPM refer to the speed of the momentum wheels associated with the case.

FSM Impact on SmallSat Jitter

In order to reduce the instrument pointing errors, the FSM places an additional torque on the spacecraft when compensating for spacecraft jitter. Assuming that additional instruments are on-board, it is important to determine the effect of this torque on the SmallSat. Table 14 shows the difference between the open-loop and closed-loop jitter environment on the SmallSat bus and the resulting increase in jitter (in dB). The increase in the uncontrolled yaw axis is equal to the increase in instrument pointing (less than 0.25 dB). A 0.05-0.20 dB increase in jitter is realized about the roll and pitch axis for each individual disturbance. The higher frequency disturbances produced by the momentum wheel imbalance have an equal impact on the SmallSat. However, the jitter associated with the high frequency disturbances is smaller and the resulting increase is less significant. The overall increase in the SmallSat jitter environment for all the disturbances is less than 1.6 dB about the roll axis and less than 0.06 dB about the pitch axis.

Table 14. SmallSat Jitter

Disturbance	Open-Loop (arcsec/sec)			Closed-Loop (arcsec/sec)			Increase in Bus Jitter (dB)		
	Roll	Pitch	Yaw	Roll	Pitch	Yaw	Roll	Pitch	Yaw
Harmonic Drive	1.833	112.350	0.208	1.847	113.061	0.213	0.07	0.05	0.21
Thermal Snap	0.813	0.054	2.462	0.830	0.054	2.464	0.18	0.06	0.01
Momentum Wheel									
X-axis only (Low RPM)	0.002	0.032	0.332	0.002	0.033	0.335	0.00	0.21	0.09
X-axis only (High RPM)	0.002	0.031	0.178	0.002	0.031	0.180	0.00	0.20	0.11
All 3 Axis (Low RPM)	0.059	0.068	0.665	0.060	0.069	0.676	0.15	0.18	0.14
All 3 Axis (High RPM)	0.054	0.064	0.356	0.055	0.066	0.363	0.16	0.19	0.16
All Disturbances									
Random-Phase (Low RPM)	2.669	112.436	3.028	3.200	113.133	2.352	1.58	0.05	-2.20
Random-Phase (High RPM)	2.684	112.429	2.898	3.215	113.145	2.193	1.57	0.06	-2.42
In-Phase (Low RPM)	2.705	112.471	3.336	2.737	113.184	3.353	0.10	0.05	0.05
In-Phase (High RPM)	2.700	112.468	3.027	2.733	113.181	3.040	0.10	0.05	0.04

* Low RPM and High RPM refer to the speed of the momentum wheels associated with the case.

Conclusions

This study was conducted to determine the feasibility of using feedback control of a FSM to reduce instrument pointing errors on a SmallSat. A mission scenario that defined the spacecraft bus, instrument, and control technology, was established in order to bound the scope of this study. A MSC/NASTRAN model of the SmallSat was constructed and an ACS was selected to define the dynamic response of the SmallSat. Disturbance sources, sensors, and actuators were identified and incorporated into the simulation. A FSM control law was designed and the effectiveness of feedback control of a FSM was accessed through simulation.

The analysis shows that instrument pointing errors about the roll and pitch axis can be significantly reduced with feedback control of a FSM. Although there is some increase in the pointing error about the yaw axis, the increase is insignificant because the transmission path length is short. The roll and pitch axis pointing errors act about a transmission path length equal to the altitude of the spacecraft and are therefore more important. The results also show that the impact on the SmallSat's jitter environment is also inconsequential. Feedback control of a FSM provides a low cost, low power solution to a problem that is typically solved by using larger reaction wheels or by devising a more sophisticated ACS, which require more power and usually higher cost. This solution provides broadband compensation without requiring apriori knowledge of the on-board disturbances (a distinct advantage over feed-forward control). For this study, the FSM control system was designed independent of the disturbance models.

The selection of quiet hardware is an important aspect in spacecraft designs. It appears, however, even with the best designs and the quietest equipment, that the science objectives of current and proposed imaging sensors are degraded because of tradeoffs made in cost and capability of hardware components. It is concluded that FSM active control technologies can be used to fill this gap for future remote sensing missions. This technology has the potential to enhance existing hardware performance and image resolution, and can create opportunities that otherwise would have been unavailable by relaxing instrument pointing requirements.

The results of this study show that instrument pointing errors can be drastically reduced with the use of a FSM without adversely affecting the SmallSat's jitter environment for other payloads. This low cost, low power solution permits an instrument more flight opportunities by allowing it to be hosted on a spacecraft that does not meet the instrument's jitter requirement. The requirement on a potential spacecraft's jitter environment could be relaxed, since the FSM can actively compensate to bring the instrument's pointing error within specifications. If instrument performance is affected by the jitter environment (i.e., imaging payloads), then active compensation with an FSM may inexpensively increase the instrument's performance.

References

[1] Johnson, Thomas A.; Nguyen, Dung Phu Chi; Cuda, Vince; Freesland Doug; Characterization of Spacecraft and Environmental Disturbances on a SmallSat; July 1994; NASA Contractor Report 194915.

[2] Wertz, James R. and Larson, Wiley J. (editors); Space Mission Analysis and Design; 1991; Kluwer Academic Publishers.

[3] Solar Activity inputs for Upper Atmospheric models; April 6, 1993; MSFC.

[4] Evaluation of CSI Enhancements for Jitter Reduction on the EOS AM-1 Spacecraft; September 13, 1993; NASA/LaRC CSIO Memorandum 93-09-01.

[5] Freesland, D. ACS Transient Response to Solar Array thermal bending; June 20, 1986; General Electric Space Division; PIR U-1K21-UARS-482.

[6] Jasper, P.E. and Neste, S.; UARS Solar Array Snap; July 9, 1986; General Electric Space Division; PIR U-1K21-UARS-481.

[7] EOS Reference Handbook; March 1993; NASA, NP-202.

[8] Hedding, Larry R. and Lewis, Robert A.; Fast steering mirror design and performance for stabilization and single axis scanning; 1990; SPIE Volume 1304 Acquisition, Tracking, and Pointing.

[9] McCormick, M.D., et al; Stratospheric Aerosol and Gas Experiment III (SAGE III) Aerosol and Trace Gas Measurements for Earth Observing System (EOS); 1991; SPIE Volume 1491, Remote Sensing of Atmospheric Chemistry.

[10] Zaremba, J.G.; A Biaxial Fast Steering Mirror for Precision Optical Pointing Systems; 1988; TRW; 88-4108-CD.

[11] Stratospheric Aerosol and Gas Experiment III (SAGE III) Description Document; NASA Langley Research Center; July 1994.

Appendix A: Simulation Results

Appendix A contains the simulation results for each disturbance. The open-loop, closed-loop (without compensation), and closed-loop (with compensation) simulation results are presented. The SmallSat ACS provides the only control for the open-loop analysis. The closed-loop (without compensation) simulation accounts for the reaction torques from the FSM as it compensates for the spacecraft jitter, but does not include FSM compensation. The closed-loop (with compensation) results account for the FSM reaction torques and incorporate the FSM control algorithms.

Case: Solar Array Harmonic Drive Axis: Roll

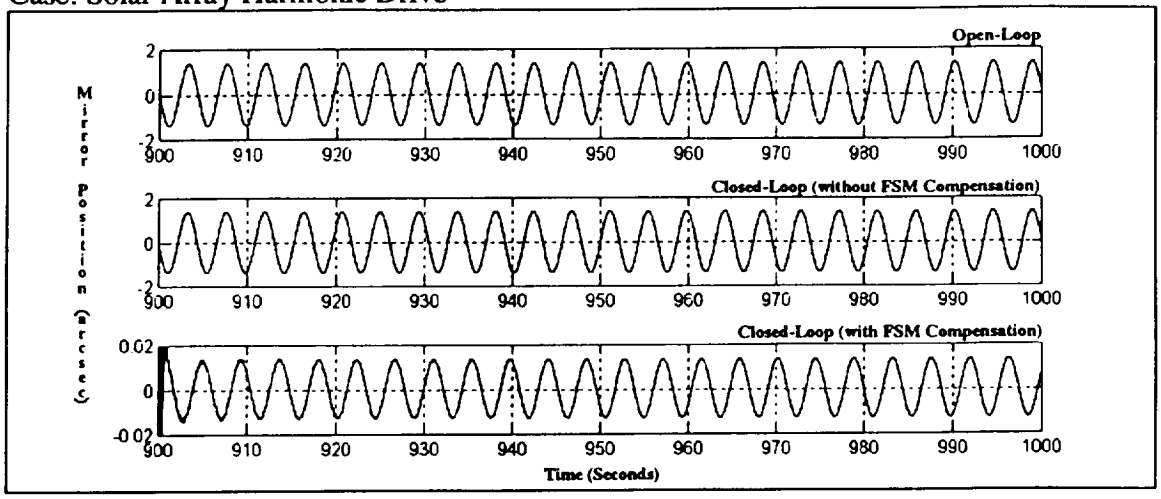

Case: Solar Array Harmonic Drive Axis: Pitch

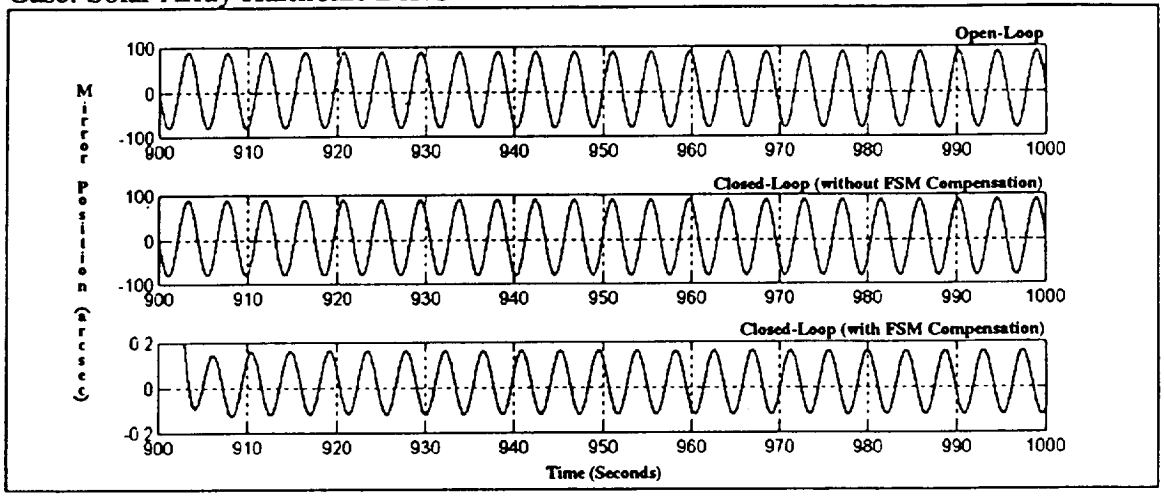

Case: Solar Array Harmonic Drive Axis: Yaw

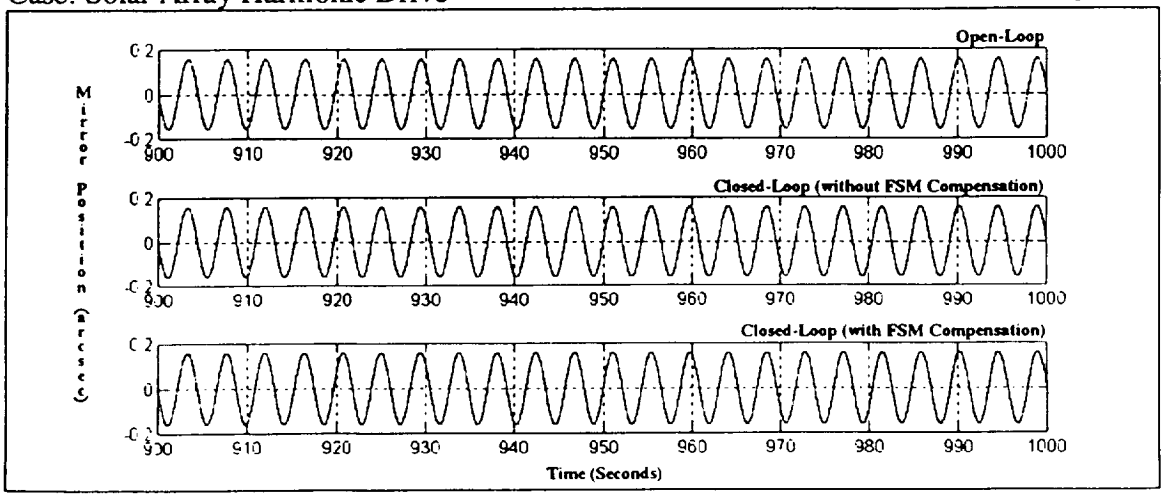

Case: Thermal Snap (disturbance 1) Axis: Roll

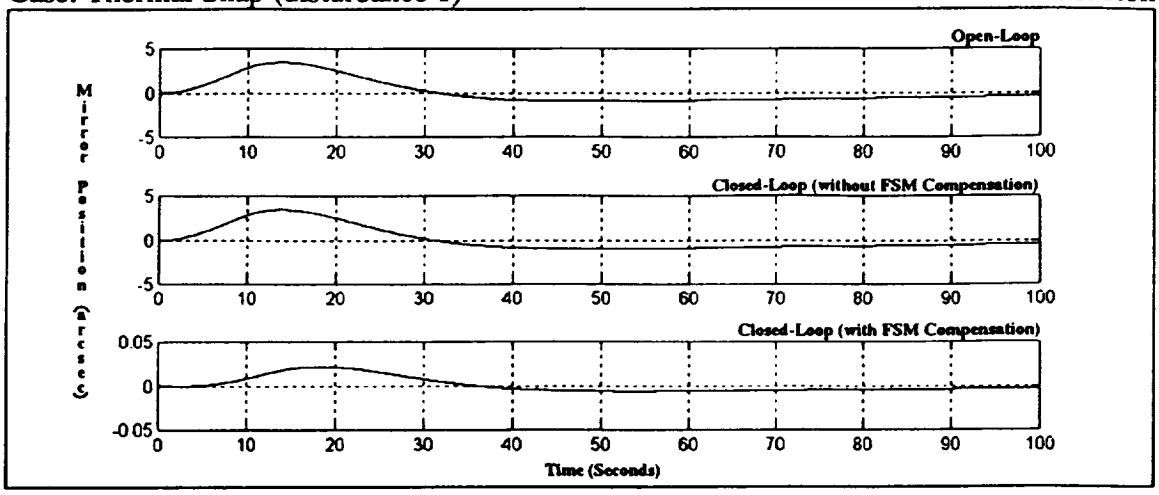

Case: Thermal Snap (disturbance 1) Axis: Pitch

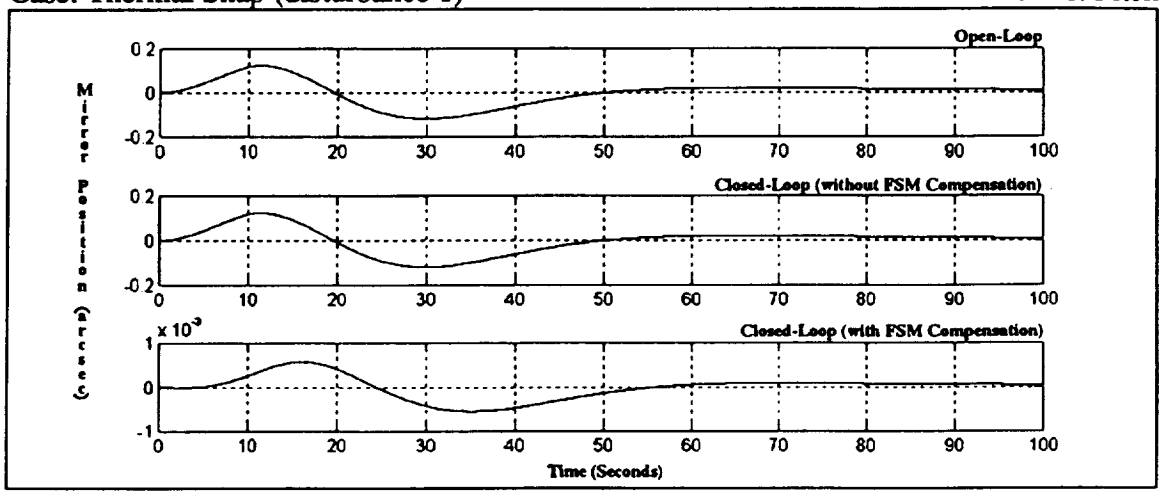

Case: Thermal Snap (disturbance 1) Axis: Yaw

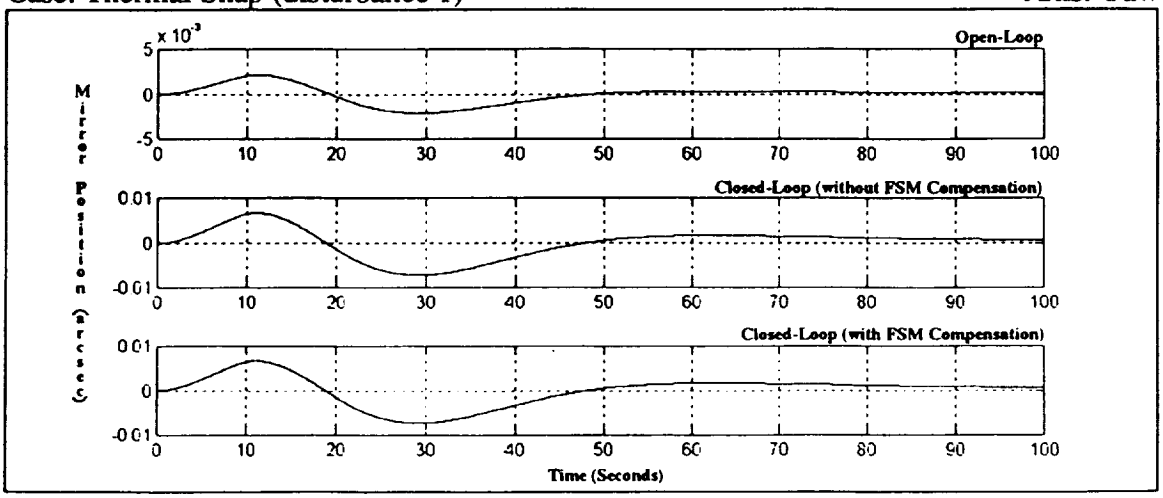

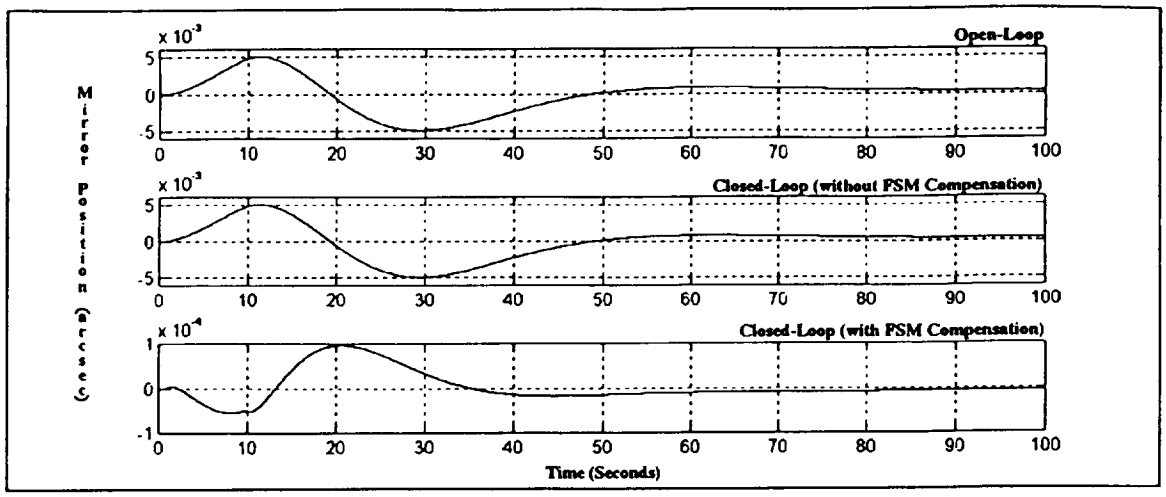

Case: Thermal Snap (disturbance 2) Axis: Yaw

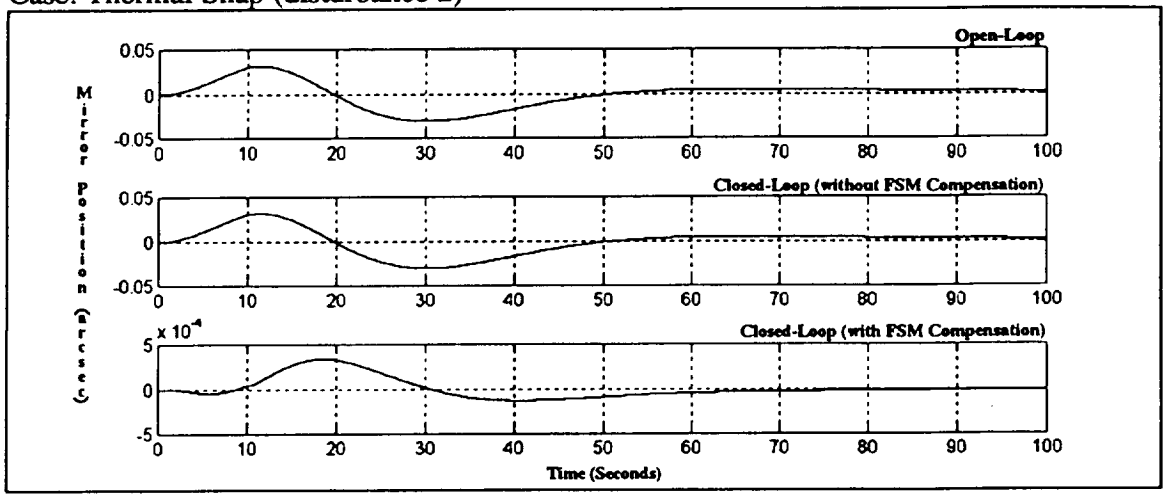

Case: Thermal Snap (disturbance 2) Axis: Yaw

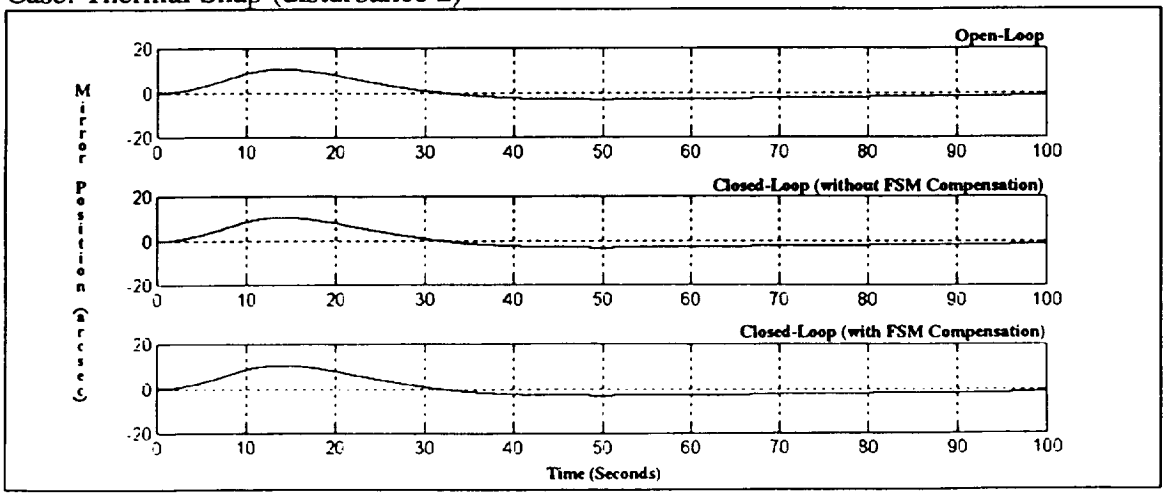

Case: All Disturbances (case 1) Axis: Roll

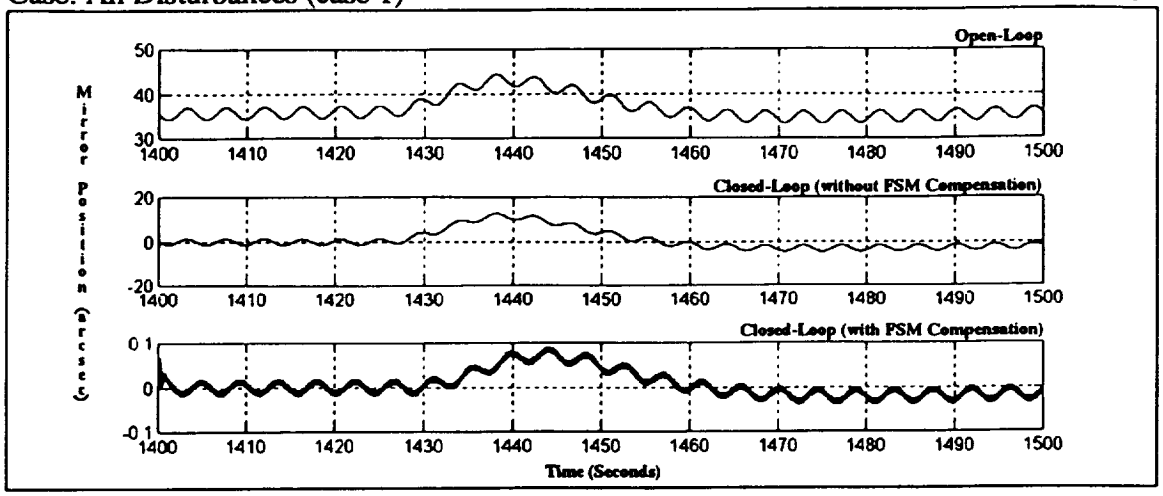

Case: All Disturbances (case 1) Axis: Pitch

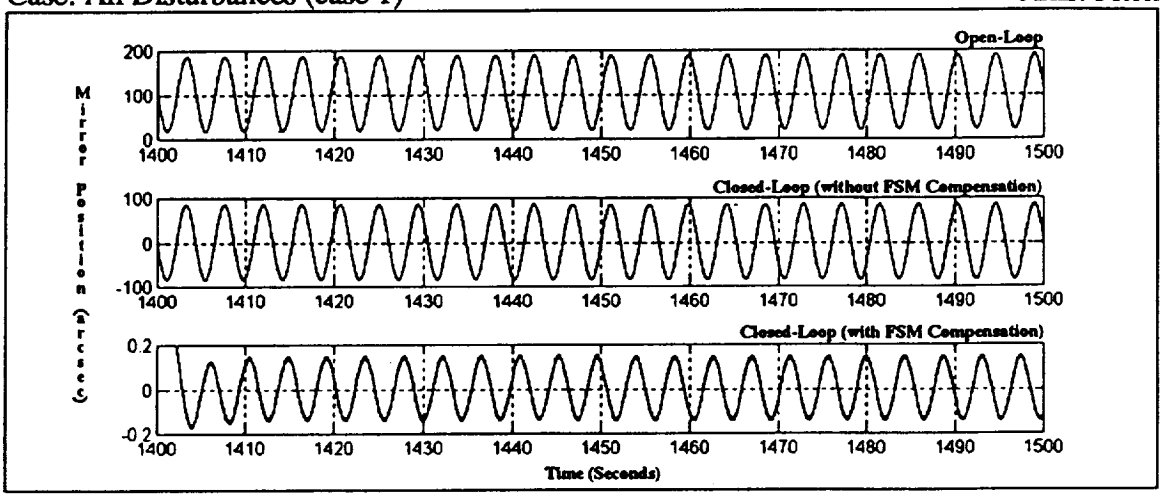

Case: All Disturbances (case 1) Axis: Yaw

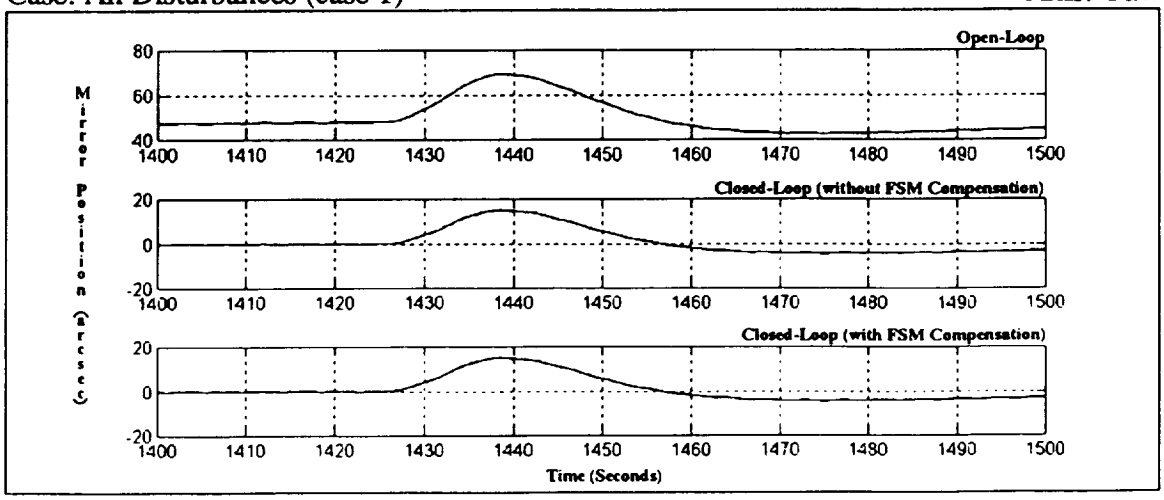

Case: All Disturbances (case 2) Axis: Roll

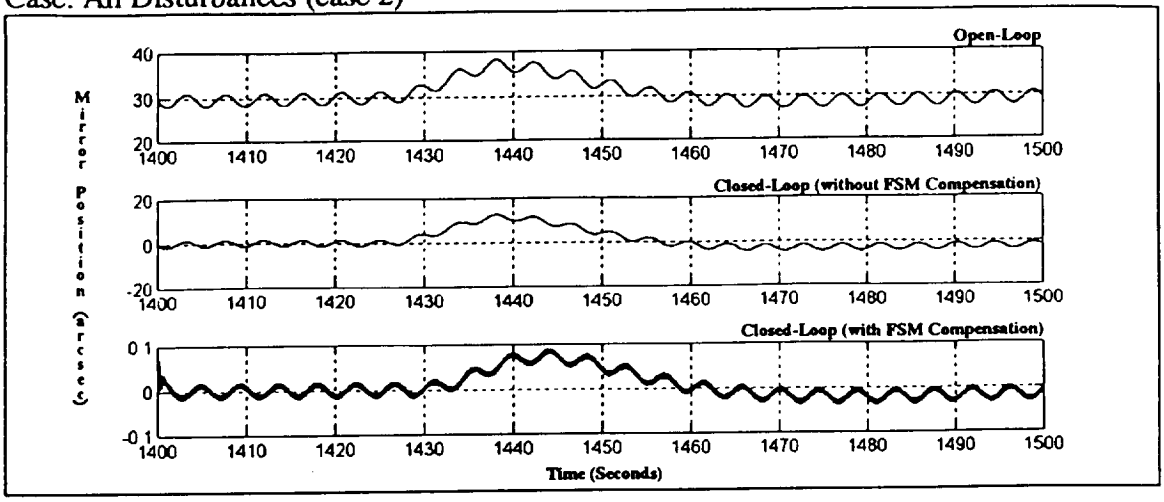

Case: All Disturbances (case 2) Axis: Pitch

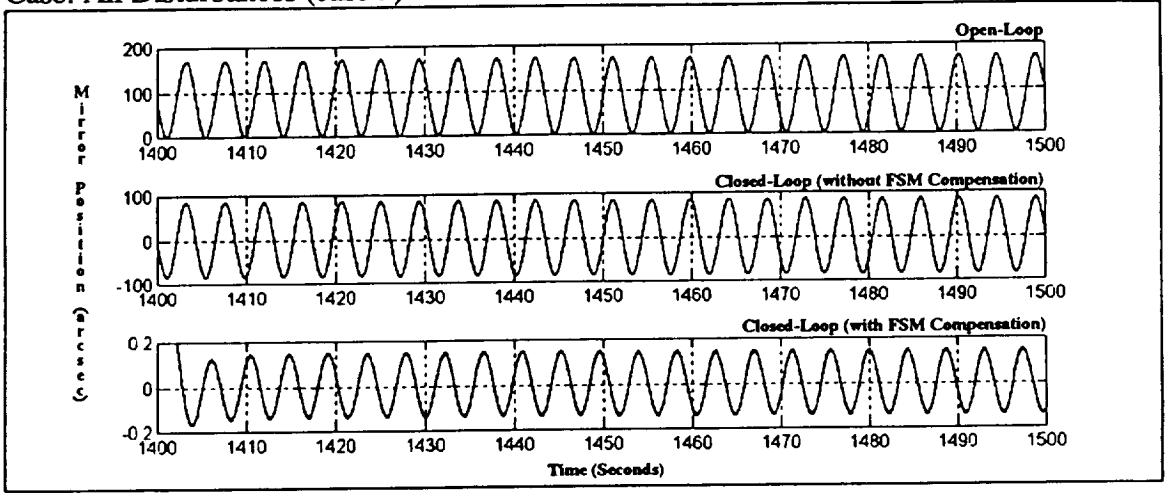

Case: All Disturbances (case 2) Axis: Yaw

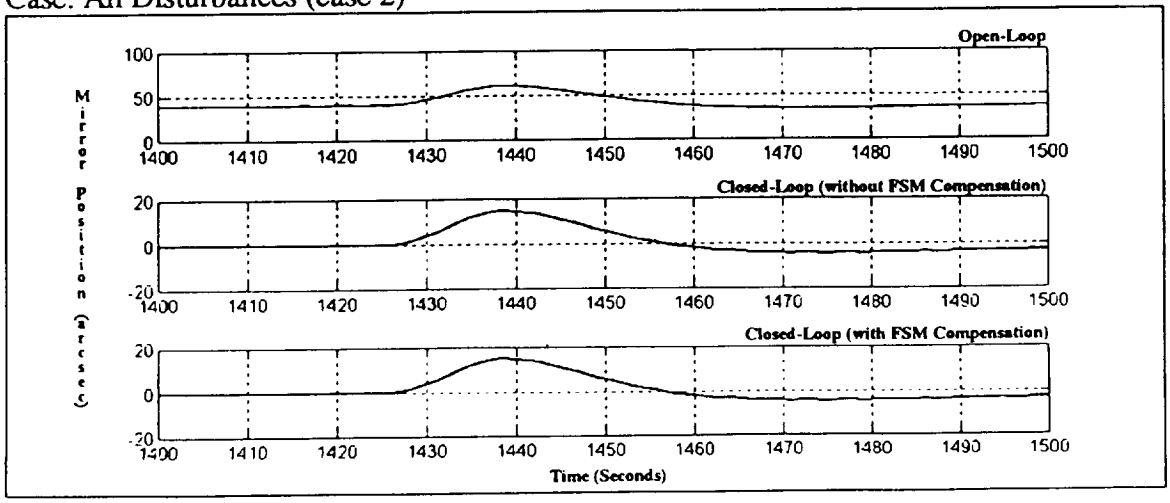

REPORT DOCUMENTATION PAGE

Form Approved
OMB No. 0704-0188

1. AGENCY USE ONLY *(Leave blank)*	2. REPORT DATE	3. REPORT TYPE AND DATES COVERED
	June 1996	Contractor Report

4. TITLE AND SUBTITLE
Using Fast-Steering Mirror Control to Reduce Instrument Pointing Errors Caused by Spacecraft Jitter

5. FUNDING NUMBERS
NAS1-18936-24

WU 233-10-14-12

6. AUTHOR(S)
Thomas A. Johnson, Jeffery Antol, Ted M. Holtz, Vince Cuda

7. PERFORMING ORGANIZATION NAME(S) AND ADDRESS(ES)
CTA Incorporated
1 Enterprise Parkway Suite 390
Hampton, VA 23666

8. PERFORMING ORGANIZATION REPORT NUMBER

9. SPONSORING / MONITORING AGENCY NAME(S) AND ADDRESS(ES)
National Aeronautics and Space Administration
Langley Research Center
Hampton, VA 23681-0001

10. SPONSORING / MONITORING AGENCY REPORT NUMBER
NASA CR-201583

11. SUPPLEMENTARY NOTES
Langley Technical Monitor: David E. Cox
Final Report

12a. DISTRIBUTION / AVAILABILITY STATEMENT
Unclassified - Unlimited

Subject Category 18

12b. DISTRIBUTION CODE

13. ABSTRACT *(Maximum 200 words)*

The scope of this study was to investigate the benefit of using feedback control of a Fast Steering Mirror (FSM) to reduce instrument pointing errors. Initially, the study identified FSM control technologies and categorized them according to their use, range of applicability, and physical requirements. Candidate payloads were then evaluated according to their relevance in use of fast steering mirror control technologies. This leads to the mission and instrument selection which served as the candidate mission for numerical modeling. A standard SmallSat was designed in order to accommodate the payload requirements (weight, size, power, etc.). This included sizing the SmallSat bus, sizing the solar array, choosing appropriate antennas, and identifying an attitude control system (ACS). A feedback control system for the FSM compensation was then designed, and the instrument pointing error and SmallSat jitter environment for open-loop and closed-loop FSM control were evaluated for typical SmallSat disturbances. The results were then compared to determine the effectiveness of the FSM feedback control system.

14. SUBJECT TERMS	15. NUMBER OF PAGES
Spacecraft jitter, Active control, Fast steering mirrors	34
	16. PRICE CODE: A03

17. SECURITY CLASSIFICATION OF REPORT	18. SECURITY CLASSIFICATION OF THIS PAGE	19. SECURITY CLASSIFICATION OF ABSTRACT	20. LIMITATION OF ABSTRACT
Unclassified	Unclassified	Unclassified	